ORIGINAL ARTICLE

Fatigue performance analysis of fine aggregate matrix using a newly designed experimental strategy and viscoelastic continuum damage theory

Zhifei Tan · Hui Li · Zhen Leng · Binbin Yin · Danning Li · Fuliao Zou · Peng Cao

Abstract Fine aggregate matrix (FAM), as the matrix phase in asphalt concrete (AC), significantly affects the fatigue behavior of AC. To accurately assess the mechanical properties of FAM, a newly designed experimental strategy for FAM testing was developed, and the viscoelastic continuum damage theory (VECD) theory was applied to analyze FAM's fatigue cracking characteristics. In this study, a dumbbell-shaped geometry for dynamic shear rheometer testing was designed and verified through the FE-aided method. Subsequently, three AC mixtures' FAM specimens with this special geometry were fabricated for the frequency sweep and linear amplitude sweep tests. Results showed that the specially designed specimens effectively capture the viscoelastic and fatigue properties of FAM with high replicability. Analyses based on the VECD theory indicated that FAM of porous asphalt (FAM(PA13)), featuring a higher asphalt content, exhibits a significant reduction in pseudo stiffness with increasing damage at the initial stage, but the reduction rate diminishes as damage progresses when compared to the other two FAMs. It was speculated that the higher aggregate content in FAM of dense-graded AC mixture (FAM(AC20) induces stress concentrations in the asphalt mastic near the protrusion areas of aggregates, thereby rendering the sample more susceptible to damage. The proposed methods will be readily extended to characterize other mechanical properties of FAM.

Z. Tan · H. Li · Z. Leng (✉) · B. Yin · D. Li · F. Zou
Department of Civil and Environmental Engineering, The Hong Kong Polytechnic University, Hong Kong, China
e-mail: zhen.leng@polyu.edu.hk

Z. Tan · H. Li · Z. Leng · B. Yin · D. Li · F. Zou
Research Center for Resources Engineering Towards Carbon Neutrality, The Hong Kong Polytechnic University, Hong Kong, China

H. Li
School of Transportation, Southeast University, Nanjing 211189, China

P. Cao
Faculty of Architecture, Civil and Transportation Engineering, Beijing University of Technology, Beijing 100081, China

1 Introduction

Fine aggregate matrix (FAM), typically composed of fine aggregates, mineral fillers, and asphalt binders [1–3], has been widely employed for evaluating the mechanical properties of asphalt binder and asphalt concrete (AC). Acting as the matrix phase of AC,

FAM fills the voids in the coarse aggregates' skeleton structure and binds them together, bridging the binder and AC [4, 5]. Commonly, the mix of asphalt binder and fillers is known as asphalt mastic, serving as the binder material in AC [6]. With the further incorporation of fine aggregates, FAM can more accurately represent the AC mixtures compared to pure asphalt binders and asphalt mastic [7–9]. Compared to AC, FAM offers time and material efficiency as it excludes coarse aggregates [10, 11]. Consequently, FAM has been extensively utilized to investigate various properties of asphalt binders, including healing [12] and aging [13, 14], as well as the fatigue cracking [6, 15, 16] and damage [17] properties of AC mixtures. These evaluations provide valuable insights into the mechanical properties of asphalt binders and AC mixtures [18–22]. Moreover, they serve as a prerequisite for the multiscale prediction of AC mixture performance [23–26].

With the increase in traffic volume, fatigue cracking has become a prevalent pavement distress that significantly reduces the service life of AC [27–29]. FAM plays a critical role in the fatigue performance of AC. This is because FAM is involved in both cohesive and adhesive failure in AC. From a mesoscopic perspective, fatigue cracking is mainly caused by adhesive failure and cohesive failure in AC. Adhesive failure refers to the separation between the coarse aggregate and the FAM, while cohesive failure occurs within the FAM [30–32]. Therefore, investigating the fatigue performance of FAM is crucial to understanding the failure of AC [18, 33]. Many studies have employed FAM to investigate the fatigue performance of AC [15, 17, 34]. Several criteria, have been introduced to determine the fatigue damage of FAMs, such as a 50% reduction in modulus [35], residual strength or strain [36, 37], dissipated energy ratio (DER) [38, 39], and ratio of dissipated energy change (RDEC) [40]. The 50% reduction in modulus is an empirical criterion, assuming the sample failed when the complex shear modulus decreased to 50% of the initial value. Both DER and RDEC are energy-based approaches, with DER considering the total dissipated energy at each cycle, while RDEC focuses on the change in dissipated energy [41, 42]. However, the analysis results based on these methods are highly dependent on loading modes and testing temperatures, limiting their applicability. Recently, the viscoelastic continuum damage (VECD) theory

has gained attention for evaluating the fatigue damage of asphalt materials, as its damage characteristics are independent of loading and temperature conditions [43–45]. Failure criteria, such as the reduction in pusudo-stiffness at the peak stress [46] and pseudo-strain energy based failure criteria [47, 48], have been proposed to evaluate the fatigue life of asphalt materials. However, few studies have applied this theory to evaluate the fatigue performance of FAMs [49, 50]. Therefore, further efforts are needed to achieve a more accurate assessment of the fatigue properties of FAM.

In the previous studies, various methods have been employed to prepare FAM materials, such as sieving the AC mixture to obtain the fine proportion [51–53], or directly preparing FAM through mix design [54, 55]. These methods result in different compositions, particularly in terms of binder content [56–58], which significantly affects the mechanical performance of AC. In terms of specimen fabrication, there is no standardized approach for creating FAM specimens for testing [59, 60]. Some studies utilize specially designed molds to create specimens with complex geometries [40, 61], while others use cored cylindrical samples from FAM specimens manufactured by the Superpave gyratory compactor [62]. These variations in sample fabrication methods and geometries have a significant impact on the quality of the prepared samples, including air void content and stress distribution, which in turn influence the measured results. It has been observed that a 1% change in air void content can lead to over a 10% reduction in modulus [63]. Therefore, more reliable FAM material preparation and specimen fabrication methods are urgently needed to reduce variability. However, there still remains a lack of an effective experimental strategy for FAM testing.

To fill this research gap, an enhanced experimental strategy for FAM was proposed in this study. The method proposed by Underwood and Kim (2013) was adopted for preparing the FAM materials [56]. This approach utilizes asphalt mastic, which is a mixture of asphalt binder and mineral filler, as the coating material. It also takes into account the absorbed binder by aggregates, making the fabricated FAM more representative of the actual FAM in AC. A new dumbbell-shaped specimen was designed through numerical modeling, and its effectiveness was validated in reducing stress concentration at the ends of the sample and

achieving a more uniform stress distribution in the middle section. The method for fabricating the FAM specimen with the designed dumbbell shape was also subsequently discussed, and fatigue tests were conducted on the fabricated specimens. The testing results were then analyzed based on the VECD theory, with the reduction in pseudo-stiffness at the peak stress utilized as the failure criterion for further calculating the fatigue life of the FAM specimen. The contributions of this study can be manifested in following aspects: (1) Designing an applicable specimen geometry for FAM testing; (2) Developing a feasible approach to fabricate FAM material and specimen for dynamic shear rheometer (DSR) testing; (3) Validating the reliability of the prepared specimens through various tests; and (4) Analyzing the fatigue cracking characteristics of FAM using the VECD theory.

2 Theoretical methodology

This section provides a concise overview of the theoretical framework and methodology employed in the present study. The initial segment introduces linear viscoelastic theory and outlines the procedure for constructing master curves. Following this, the VECD theory and the approach for determining the fatigue life of FAM are elucidated. The methodologies presented herein will be applied to assess the viscoelastic and fatigue characteristics of the three examined FAMs.

2.1 Linear viscoelasticity and master curve construction

Asphalt binder and its mixes are commonly regarded as viscoelastic materials, which can be described by the following constitutive relationship [64]:

$$\sigma(t) = \int_0^t G(t - \xi)\frac{d\gamma(\xi)}{d\xi}d\xi \tag{1}$$

where t is time, and ξ is a time variable of integration; $G(t)$ is the relaxation modulus in shear. For numerical computation, $G(t)$ is generally expressed as the format of the Prony series, which is known as Prony series model or generalized Maxwell model and can be written as below [65, 66]:

$$G(t) = G_\infty + \sum_{i=1}^N G_i e^{-t/\rho_i} \tag{2}$$

where N is the total number of Maxwell elements; G_∞ is the equilibrium shear modulus; G_i and ρ_i are the shear modulus and relaxation time of i th Maxwell element. G_i and ρ_i are the parameters of Prony series model, and once determined, the Prony series model becomes fully characterized. Commonly, the FS test is employed to quantify the viscoelastic properties of asphalt materials. To derive the parameters of the Prony series model, a Fourier transform is conducted to convert Eq. (2), the Prony series in the time domain, into the frequency domain, as expressed below [67]:

$$G^*(\omega) = G'(\omega) + jG''(\omega) \tag{3}$$

$$G'(\omega) = G_\infty + \sum_{i=1}^N \frac{G_i\rho_i^2\omega^2}{1 + \rho_i^2\omega^2} \tag{4}$$

$$G''(\omega) = \sum_{i=1}^N \frac{G_i\rho_i}{1 + \rho_i^2\omega^2} \tag{5}$$

where j is the imaginary unit ($j = \sqrt{-1}$); G^*, $G\prime$, and G'' are complex modulus, storage modulus and loss modulus in shear, respectively. ω is the angular frequency.

From the FS test, $G\prime$, and G'' within a narrow frequency range from 0.1 Hz to 100 Hz at the measured temperature can be obtained. To extend the frequency range, frequency sweep tests at different temperatures should be conducted, and the acquired data are shifted based on the time–temperature superposition principle (TTSP). This allows the construction of master curves at a reference temperature (T_r) over a wide frequency range by shifting the actual frequency (ω) to the reduced frequency (ω_r):

$$\omega_r = \omega \times \alpha_T \tag{6}$$

where α_T is the shift factor. For FAM, the Williams-Landel-Ferry (WLF) equation, as shown below, is commonly adopted:

$$\log(\alpha_T) = -\frac{C_1(T - T_r)}{C_2 + (T - T_r)} \tag{7}$$

where C_1 and C_2 are the model parameters.

Furthermore, the shifted data points should be further smoothed to derive the master curves in a wide frequency range. In this study, the modified Huet Sayegh (MHS) is adopted to fit the shifted data. The mathematic expression of the MHS is as below [68]:

$$D^*(\omega)_{MHS} = \frac{G'(\omega)_{HS}}{|G^*(\omega)_{HS}|^2}$$
$$- j\left[\frac{G''(\omega)_{HS}}{|G^*(\omega)_{HS}|^2} + \frac{1}{\eta_3\omega}\right] = D'(\omega)_{MHS}$$
$$- jD''(\omega)_{MHS} \tag{8}$$

where $D^*(\omega)_{MHS}$, $D\prime(\omega)_{MHS}$ and $D''(\omega)_{MHS}$ are the complex, storage and loss creep compliances of the MHS model, respectively; $G^*(\omega)_{HS}$, $G\prime(\omega)_{HS}$ and $G''(\omega)_{HS}$ represent the complex, storage and loss moduli of the original Huet Sayegh (HS) model [69], respectively. η_3 is the linear dashpot parameter. In this model, a linear dashpot is placed in series with the original and thus it can improve the fitting at the low frequency region. Based on the relationship between creep compliance and modulus, the storage modulus and loss modulus of the MHS model can be calculated as follows:

$$G'(\omega)_{MHS} = \frac{1}{D'(\omega)_{MHS}} \tag{9}$$

$$G''(\omega)_{MHS} = \frac{1}{D''(\omega)_{MHS}} \tag{10}$$

By optimizing the parameters of the WLF function and MHS model, the master curves of FAM over a wide frequency range can be developed.

2.2 Viscoelastic continuum damage (VECD) model

The VECD model is a commonly used method for evaluating the fatigue damage of asphalt materials [43, 70]. This model employs the elastic–viscoelastic correspondence principle, proposed by Schapery in 1984 [71], to equate the viscoelastic constitutive equations to elastic ones through the concept of pseudo strain. This allows the elimination of the viscous effect. The pseudo strain can be calculated using the following convolution integral:

$$\gamma^R(t) = \frac{1}{G^R}\int_0^t G(t - \xi)\frac{\partial\gamma}{\partial\xi}d\xi \tag{11}$$

where γ^R is the pseudo strain in shear; G^R is a reference shear modulus, which is selected to be unity; $G(t)$ is the relaxation shear modulus; t and ξ are time and time integration variable.

To characterize the damage evolution with the increase of loading time, two parameters, including pseudo stiffness (C) and damage parameter (S) were proposed. C is defined as the deviation of the stress from the pseudo strain and it can be calculated as follows:

$$C(t) = \frac{\tau(t)}{\gamma^R(t)} \tag{12}$$

where τ is the shear stress. The damage parameter, S, is defined as an internal state variable, which is used to describe the damage growth in the sample. This parameter is correlated to pseudo strain energy (W^R) based on Schapery's work potential theory by the following expression [72]:

$$\frac{dS}{dt} = \left(-\frac{\partial W^R}{\partial S}\right)^\alpha \tag{13}$$

where W^R is the pseudo strain energy density function; α is a constant of the damage growth rate, which is equal to $(1 + 1/m)$, in which m is the maximum slope of the relaxation modulus ($G(t)$) with time in the log–log scale. To acquire $G(t)$ curve at time domain, the developed master curve based on the MHS model (Eqs. 8–10) in the frequency domain is employed to optimize the parameters of the Prony series model through regression analysis. This is achieved by minimizing the error between the master curves (storage and loss moduli) calculated by the MHS model and the Prony series model (Eq. 3–5). Once the parameters of Prony series are determined, $G(t)$ can be derived using Eq. (2) and thus m, the maximum slope of $G(t)$ can be obtained for the plot. To determine the W^R, the pseudo strain energy density in Eq. (13), the following equation proposed by Kim et al. for AC under uniaxial tension loading is adopted [73]:

$$W^R = \frac{DMR}{2}C(S) \times (\gamma^R)^2 \tag{14}$$

where pseudo stiffness (C) is expressed as a function of damage (S); DMR, equal to $|G^*|_{\text{fingerprint}}/|G^*|_{\text{LVE}}$, is the dynamic modulus ratio, which is used to reduce the effect caused by the sample's variation. $|G^*|_{\text{LVE}}$ is the dynamic shear modulus; and $|G^*|_{\text{fingerprint}}$ can be determined by the frequency sweep test before the LAS test. Plugging Eq. (14) into Eq. (13) and using the chain rule $\left(\frac{dC}{dt} = \frac{dC}{dt} \times \frac{dt}{dS}\right)$, the following relations can be obtained for the damage parameter (S):

$$\frac{\mathrm{d}S}{\mathrm{d}t} = \left[-\text{DMR}\frac{\left(\gamma^R\right)^2}{2}\frac{\mathrm{d}C}{\mathrm{d}t}\right]^{\frac{\alpha}{1+\alpha}} \tag{15}$$

$$S = \int_0^t \left(-\text{DMR}\frac{\left(\gamma^R\right)^2}{2}\frac{\mathrm{d}C}{\mathrm{d}t}\right)^{\frac{\alpha}{1+\alpha}}\mathrm{d}t \tag{16}$$

Since C and γ^R both are functions of t, Eq. (16) is implicit and cannot be calculated directly. By using the chain rule ($\frac{dC}{dt} = \frac{dC}{dS}\frac{dS}{dt}$) again, the following numerical approximation is derived to compute S:

$$S = \sum_{j=1}^N \left[\left(\frac{\text{DMR}}{2}\left(\gamma^R\right)^2\left(C_{j-1} - C_j\right)\right)^{\frac{\alpha}{1+\alpha}}\left(t_j - t_{j-1}\right)^{\frac{1}{1+\alpha}}\right] \tag{17}$$

where N is the total cyclic number; C_j and t_j are the pseudo stiffness and time at j th cycle. γ^R in Eq. (17) from the uniaxial test can be replaced by the peak pseudo strain (γ_p^R) in the cyclic test. Thus, the damage in cyclic tests can be expressed as follows:

$$S = \sum_{j=1}^N \left[\left(\frac{\text{DMR}}{2}\left(\gamma_p^R\right)^2\left(C_{j-1} - C_j\right)\right)^{\frac{\alpha}{1+\alpha}}\left(t_j - t_{j-1}\right)^{\frac{1}{1+\alpha}}\right] \tag{18}$$

and the peak pseudo strain (γ_p^R) can be expressed as follows:

$$\gamma_p^R = \frac{1}{G^R} \times |G^*|_{\text{LVE}}\gamma_p \tag{19}$$

In this study, the experimental data from the LAS test is used to analyze the fatigue damage. In order to further calculate the fatigue life of samples at a certain strain level (γ), Eq. (20) is used [74]:

$$N_f = A\left(\frac{1}{G^R}\gamma \cdot |G^*|_{\text{LVE}}\right)^{-B} \tag{20}$$

$$A = \frac{f \cdot \left(S_f\right) \cdot 2^\alpha}{k \cdot \left(C_1 C_2\right)^\alpha} \tag{21}$$

$$B = 2\alpha \tag{22}$$

$$k = 1 - \alpha \cdot C_2 + \alpha \tag{23}$$

$$S_f = \left(\frac{1 - C@\text{Peak stress}}{C_1}\right)^{1/C_2} \tag{24}$$

where S_f is the failure criterion based on pseudo-strain energy; it corresponds to the reduction in pseudo stiffness (C) at the peak stress. C_1 and C_2 are the two parameters of pseudo stiffness ($C(S)$) fitted by the following exponential function:

$$C(S) = 1 - C_1 S^{C_2} \tag{25}$$

For cyclic tests at a certain strain, $C(S)$ can be calculated by following equation [43]:

$$C(S) = \frac{\tau_p}{\gamma_p^R} \tag{26}$$

Thus, by fitting the calculated $C(S)$ based on experimental data with Eq. (7), both parameters, i.e., C_1 and C_2 can be determined.

3 Computational design of FAM specimen

In this section, a dumbbell geometry for the FAM measurement is proposed. Besides, numerical modeling is conducted to determine the geometric parameters in the DSR testing. Further, the characteristics of stress distribution in the sample are also analyzed.

3.1 Geometric design

A well-designed geometry should be able to reasonably evaluate material properties and satisfy DSR requirements, such as maximum torque. As depicted in Fig. 1, a dumbbell-shaped geometry is proposed. The total height of the geometry is 26 mm. The middle straight section with a 6 mm diameter is the predefined zone for the property evaluation. The middle straight section smoothly transmits to the two ends with a curve with a radius of 5 mm. This geometry
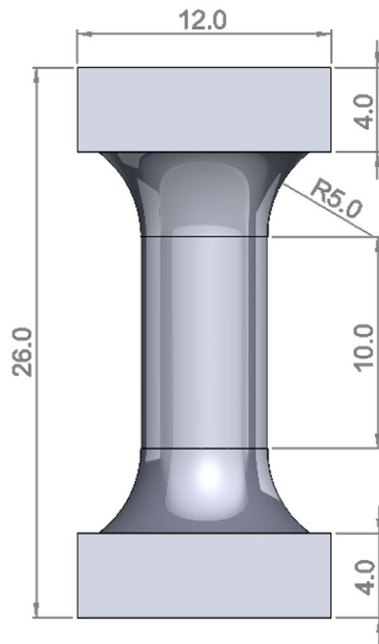
Fig. 1 The geometry of the designed FAM specimen

has been widely used in testing metal materials [75]. However, unlike the testing sample for metal materials, steel rings are attached to the two ends and bound with the FAM material to fix the sample on the DSR tightly. The use of rings is necessary as the FAM material is too soft, and the rings ensure that the applied torque by the DSR can be effectively transferred to the test sample. Compared to the commonly used cylindrical column shape for FAM testing, the proposed dumbbell geometry has a distinct advantage. The cylindrical column shape often experiences stress concentration at both ends due to the constraints, leading to inaccurate testing results and even fracture at the ends during the damage test. The dumbbell geometry solves this issue by connecting the two ends with a transition section, which can significantly reduce the effect of constraints at both ends, thereby providing more accurate testing results. This advantage will be verified in the following section. Additionally, despite the existence of studies proposing similar designs with transition section from the middle to the end, the marginal increments in radii are often insufficient, resulting in insignificant stress reduction and posing challenges in fabrication, particularly for FAM with larger particles [61]. Furthermore, certain geometries incorporating a varying

cross-section along the height of the specimen [40], such as the dog-bone shape proposed by Apostolidis et al. [76, 77], have been adopted, but the response of the sample may vary at different locations of the specimen. Nevertheless, it should be acknowledged that the proposed geometry may still have certain limitations. For instance, it might not be suitable for testing severely aged FAM. Despite these limitations, the proposed geometry is anticipated to be more applicable and yield more accurate testing results in the evaluation of FAM properties. The feasibility of this geometry is assessed through numerical modeling in the following section.

4 Numerical validation

4.1 Parametric study on FAM geometry

The transition zone significantly influences the stress distribution in FAM specimens. Thus, a parametric study on the neck radius is required. For this purpose, a numerical investigation was conducted on geometries with neck radii ranging from 0 to 5 mm, while keeping the end radius (5 mm) and length (26 mm) constant. In the simulation, the FAM material was treated as a homogeneous material with shear modulus and Poisson's ratio set at 100 MPa and 0.45, respectively. The steel rings were fixed at both ends, and the bottom steel ring was constrained. A torque (T) of 70 N·mm was applied to the top steel ring. Figure 2a illustrates the shear stress distribution for specimens with varying neck radii. It is evident that an increase in neck radii results in reduced stress concentration at both ends. To quantify this effect, ratios of stress at the neck (S23_Neck) to stress at the middle (S23_Middle) were evaluated, as depicted in Fig. 2b. The stress ratio decreases from 1.77 to 1.05 with increasing neck radii from 0 to 5 mm. The significantly lower stress ratio for the geometry with a neck radius of 5 mm proves the effectiveness of stress concentration reduction for the adopted geometry.

4.1.1 Determining geometric parameters for DSR measurements

Since the cylindrical sample is used in the standard DSR test, the physical geometry of the dumbbell sample cannot be directly used in DSR testing, and it
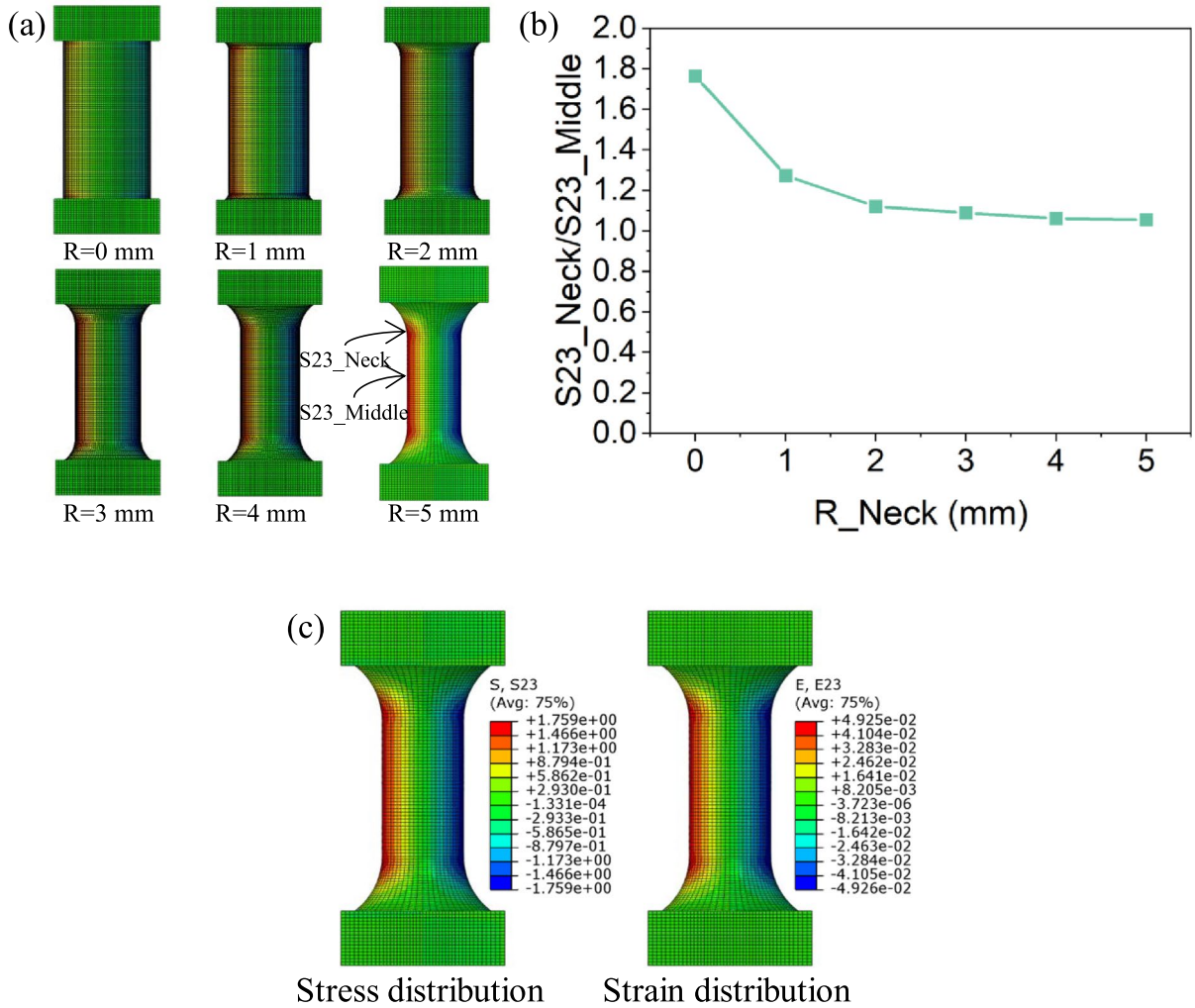
Fig. 2 Effect of neck radius on the stress concentraion of specimen: **a** shear stress (S23) distributions for specimens with different neck radii; **b** concentration ratio (S23_Neck/S23_Middle); and **c** stress and strain distributions on the designed specimen

should be equivalent to the standard cylindrical shape. The equivalent radius and height are named effective radius and effective height. As the radius of the middle section of the sample, the targeted zone in measurement is equal to 3 mm. Therefore, this radius is used as the effective radius for this geometry. The effective height of the specimen is further calculated based on the numerical simulation results of the designed geometry. For a cylindrical sample under a shear torque, the shear stress and shear strain can be expressed as follows:

$$\tau = k_1 \frac{2T}{\pi R_{eff}^3} \tag{27}$$

$$\gamma = \frac{\theta \cdot R_{eff}}{h_{eff}} \tag{28}$$

where T is the applied torque; τ and γ is shear stress and shear strain; k_1 is a constant; R_{eff} is the effective radius, which is 3 mm in this study; θ is the rotated angle; and h_{eff} is the effective height of the test specimen.

Figure 2c illustrates the distribution of shear stress and shear strain in the designed geometry, while the average shear stress (τ) and shear strain (γ) on the surface of the middle straight section were computed as 1.648 MPa and 0.046, respectively. By utilizing Eq. (27) and (28), k_1 and h_{eff} were calculated, which

were 0.998 and 15.506 mm, respectively. Therefore, the determined three parameters, including k_1, effective radius (R_{eff}), and effective height (h_{eff}) were used as the geometrical parameters for the adopted geometry in DSR measurements.

4.1.2 Stress distributions

A comparative analysis is conducted between the proposed geometry and the commonly used cylindrical specimen in order to evaluate the effectiveness of the designed geometry. To this end, a model is developed for the cylindrical sample, and the modeling results are compared with those obtained for the proposed geometry. Von Mise stress distributions for both geometries are shown in Fig. 3 when subjected to the same shear torque. The results indicate that high stress concentrations occur in the middle section of the designed geometry, whereas for the conventional cylindrical specimen, they are concentrated at the two ends. This difference suggests that the designed geometry can significantly reduce the constraint effect of the two ends on the targeted middle sections, thereby enhancing the reliability of measurements.

4.2 Mold fabrication

To accommodate the geometry's changing radius, a specially designed mold is required to fabricate the FAM specimen. Figure 4a and b show the geometry of the mold and the assembled mold, respectively. Considering its superior thermal stability and anti-adhesion properties, Teflon is chosen as the mold material. The mold is divided into two parts at the middle section and can be easily assembled

Fig. 3 Von Mises stress distributions in the **a** conventional cylindrical specimen; and **b** dumbbell specimen
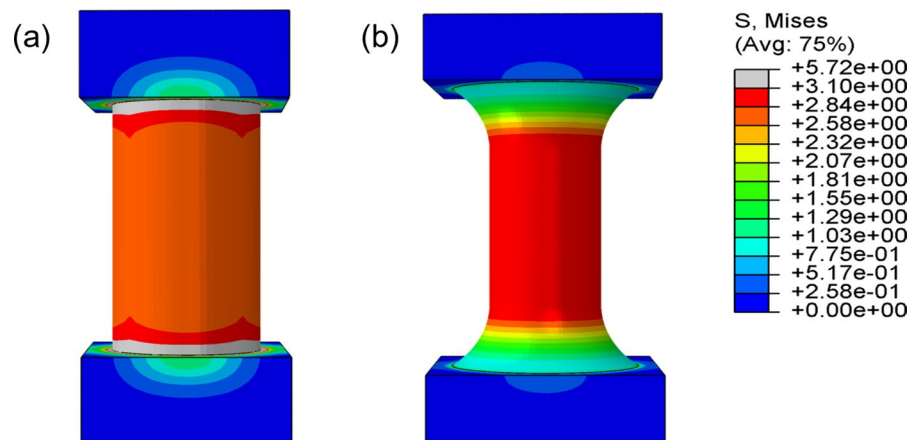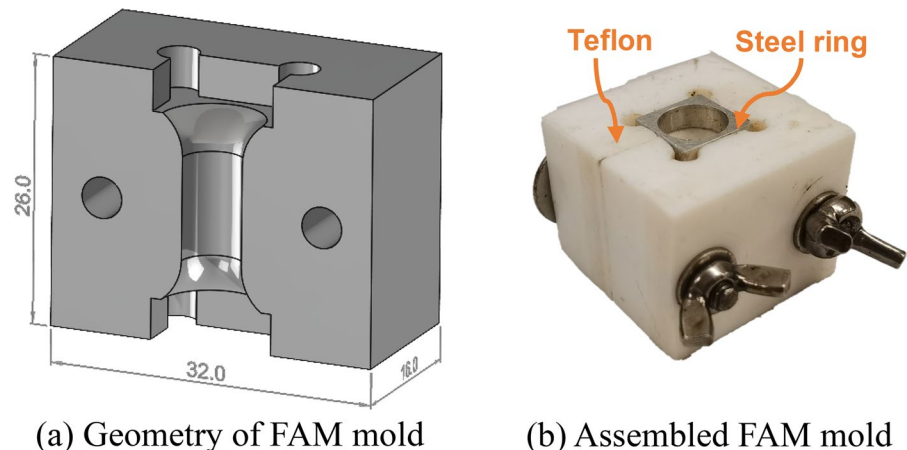
Fig. 4 The designed mold for preparing the FAM specimen

(a) Geometry of FAM mold   (b) Assembled FAM mold

by screws, which simplifies the removal of the FAM sample from the mold after fabrication.

5 Sample preparation

This section outlines the preparation of the FAM material, sample fabrication, and the mechanical measurements of the fabricated specimen.

5.1 FAM material preparation

The FAM materials used in this study were prepared based on three common AC mixtures in Hong Kong, namely, gap-graded SMA10, dense-graded AC20, and open-graded PA13. The SMA10 and PA13 mixtures employed a styrene–butadiene–styrene (SBS) modified binder with a Superpave performance grade of 76–16 (PG76-16). The AC20 mixture used a virgin asphalt binder with a penetration grade of 60/70 (Pen60/70). The binder contents for SMA10, AC20, and PA13 were 6.0%, 5.2%, and 6.0%, respectively. In this study, the mix design method was utilized to prepare the FAM materials rather than the traditional sieving method. The mix design method is preferred due to its convenience and ability to control the compositions of the fabricated FAM materials. In this method, fine aggregates smaller than 2.36 mm, mineral fillers, and asphalt binders were considered the components of the FAM [25]. The Underwood and Kim (2013) method was adopted to determine the compositions of the three FAMs [78]. This approach considers the asphalt mastic, a mix of asphalt binder and mineral filler, as the coating material in the calculation, which is consistent with the actual AC mixture. Furthermore, this method deducts the absorbed binder by aggregates, making the fabricated FAM more equivalent to that in the real AC mixture.

In this method, the essential task is to determine the thickness of coated mastic film (t). If the mastic content is known, the compositions of the FAM can be entirely determined. To this end, the effective binder (M_{be}) in the AC mixture is calculated by using the total asphalt binder (M_b) minus the total absorbed asphalt binder (M_{ba}). Based on the mass of effective binder and mineral filler, a theoretical volume ($V_{mastic,JMF}$) of mastic based on the given gradation (job mix formula) can be calculated by adding the volume of effective binder (V_{be}) and mineral filler ($V_{0.75}$) as shown below:

$$V_{mastic,JMF} = V_{be} + V_{0.75} \tag{29}$$

Besides, the volume of asphalt mastic can also be calculated by assuming all the spherical particles coated by mastic films with the same thickness t:

$$V_{mastic,i} = \frac{\pi}{6}\left[\left(\frac{d_{i+1} + d_i}{2} + 2t\right)^3 - \left(\frac{d_{i+1} + d_i}{2}\right)^3\right] \tag{30}$$

$$V_{mastic,calc} = \sum_{i=1}^{J}\left[N_i \times V_{mastic,i}\right] \tag{31}$$

where $V_{mastic,i}$ and $V_{mastic,calc}$ are the volumes of mastic coated on a single particle and all particles, respectively; d_i and d_{i+1} are the sieve sizes of sieve i and sieve $i + 1$; N_i is the number of particles retained in sieve i. J is the total number of sieves. The mastic film thickness t can be founded by making $V_{mastic,calc}$ equal to $V_{mastic,JMF}$. Thus, the compositions of the FAM can be determined accordingly. The detailed calculations can be found in the reference [78].

The corresponding compositions of the three studied FAMs can be determined, as presented in Table 1. The calculated binder contents for FAM (AC20), FAM (SMA10), and FAM (PA13) were 9.5%, 21.1%, and 29.3%, respectively. AC20, with the highest fraction of fine aggregates, resulted in the lowest binder content of FAM (AC20).

The three FAMs were fabricated in the laboratory according to their compositions. For each FAM, 500 g of material was prepared. Mineral filler, fine aggregates (< 2.36 mm), and asphalt binder were preheated in an oven at the mixing temperature for one hour. Then, the fine aggregates were mixed with asphalt binder in a mixer for 5 min, after which the

Table 1 Mass compositions (%) of the three studied FAM materials

Size (mm)	FAM(AC20)	FAM(SMA10)	FAM(PA13)
1.18 ~ 2.36	25.3	11.9	12.7
0.6 ~ 1.18	17.5	4.0	12.1
0.3 ~ 0.6	15.6	7.9	12.1
0.15 ~ 0.3	11.7	7.1	11.4
0.075 ~ 0.15	6.6	5.2	10.8
Mineral filler	13.8	42.7	11.6
Binder content (%)	9.5	21.1	29.3

mineral filler was added and mixed for an additional 5 min. Finally, the loosened FAM material was put back into the oven for half an hour to simulate short-term aging. These prepared FAM materials were utilized in the subsequent section for DSR testing.

5.2 FAM sample fabrication

In the fabrication of dumbbell specimens for testing, it is crucial to control air voids in the specimen, as they significantly impact the mechanical performance of FAM. Although air voids naturally occur in FAM for real asphalt mixtures, our study is oriented towards achieving the minimal air void content in FAM. Several considerations motivate this approach. Firstly, it is still unclear how much air void in AC should be considered in FAM. Secondly, due to the elevated asphalt binder content in FAM, the anticipated air voids within FAM are expected to be relatively low, with the majority of air voids in asphalt mixtures manifesting as large optical voids. Thirdly, air voids are conventionally treated as a phase in numerical modeling, rendering properties measured on FAM without air voids more suitable for subsequent simulation. Lastly, the introduction of air voids into small specimens may complicate quality control during fabrication, potentially leading to increased variations in test results.

Figure 5 illustrates the fabrication of dumbbell samples using a designed mold. The following steps were undertaken to produce the samples:

(1) The mold was assembled and fixed on a frame (Fig. 5a). Then the mold was preheated in an oven of 180 °C for one hour (Fig. 5b). Simultaneously, the raw FAM material was shaped into small strips on a hot pan at around 90 °C (Fig. 5c).

(2) Once the mold was preheated, the strips were inserted into the mold (Fig. 5d) and left in the oven for five minutes. The preheated steel bar was then used to compact the sample from the top to evacuate any cavities in the mold. This step
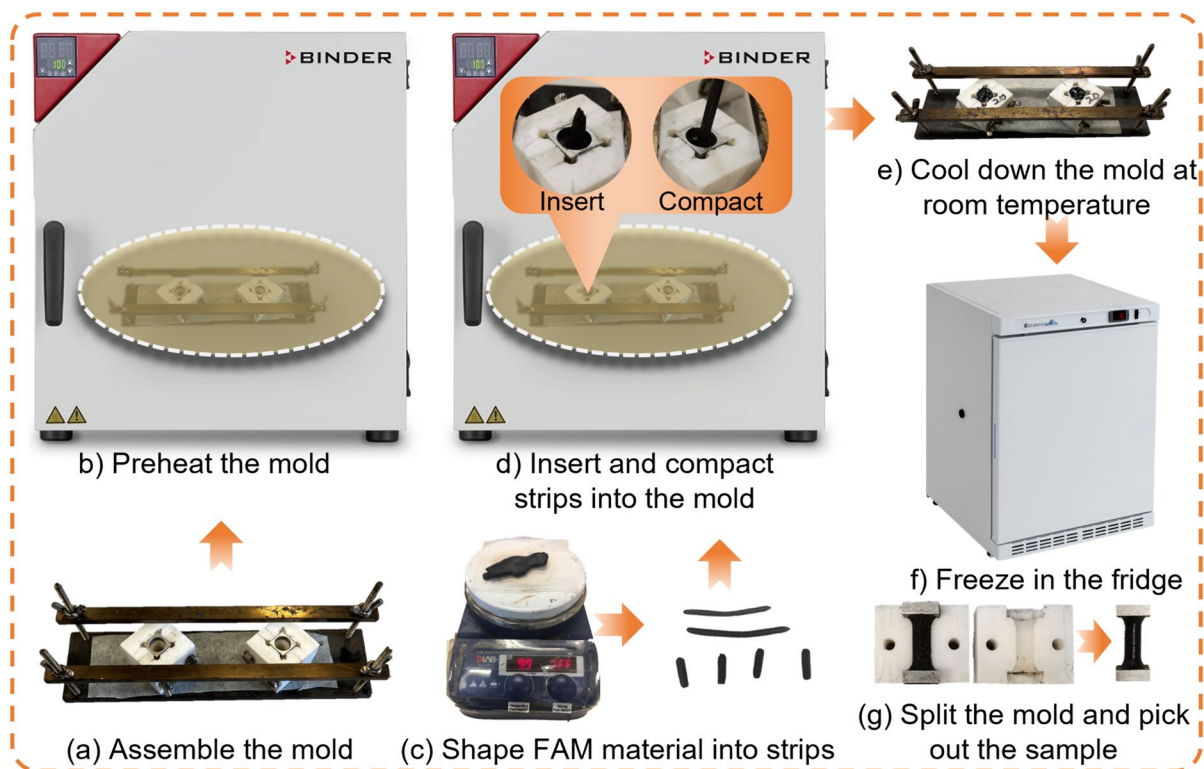

Fig. 5 FAM sample preparation

was repeated around three times until the mold was filled with the FAM material.

(3) The mold was then taken out from the oven and cooled to ambient temperature (Fig. 5e) before being transferred to a fridge at -10 °C for two hours (Fig. 5f).

(4) After cooling, the mold was removed from the fridge, and the screws were released, allowing the mold to be split down the middle using a small knife. The specimen was then carefully removed from the mold (Fig. 5g).

The air void contents of the fabricated samples were measured to evaluate their quality. Due to the smooth surface of the specimens prepared using the designed mold, the volume of the sample ($V_{\text{FAM}} = 1769.06$ mm^3) could be accurately calculated using the sample's geometry. The mass of the FAM material (M_{FAM}) in each sample was then determined by subtracting the mass of the two steel rings from the total mass of the sample. Thus, the air void content (P_a) of the FAM samples was subsequently calculated using the following equations:

$$G_{\text{mb}} = \frac{M_{\text{FAM}}}{V_{\text{FAM}}} \tag{32}$$

$$P_a = 1 - \frac{G_{\text{mb}}}{G_{\text{mm}}} \tag{33}$$

where G_{mb} and G_{mm} are the bulk density and maximum density of FAM material, respectively. The average air void content of the prepared samples was determined to be 1.85%, with a standard deviation of 0.5%. While this variation may not be significant, it is recommended to weigh the mass of the samples before conducting tests to ensure accurate results.

6 Experimental tests

In this section, the setup of the DSR measurement for the designed specimen is detailed, which is widely used to perform the testing on FAM as it is versatile and requires only a tiny amount of material [3, 10]. The two tests, namely the frequency sweep (FS) test and the linear amplitude sweep (LAS), are introduced. The two tests can be used to measure the linear viscoelastic (LVE) and fatigue properties of the three studied FAMs.

6.1 DSR measuring system

Mechanical tests on FAM specimens were performed using an Anton Paar DSR (model MCR 702), capable of applying torque ranging from 0.1 to 200 mN·m at a frequency ranging from 10^{-6} to 150 Hz and controlling the temperature from -150 to 550 °C. The setup for the DSR testing is displayed in Fig. 6, wherein fixtures with a sample clamping system are used for the measurement. To set up the sample for testing,
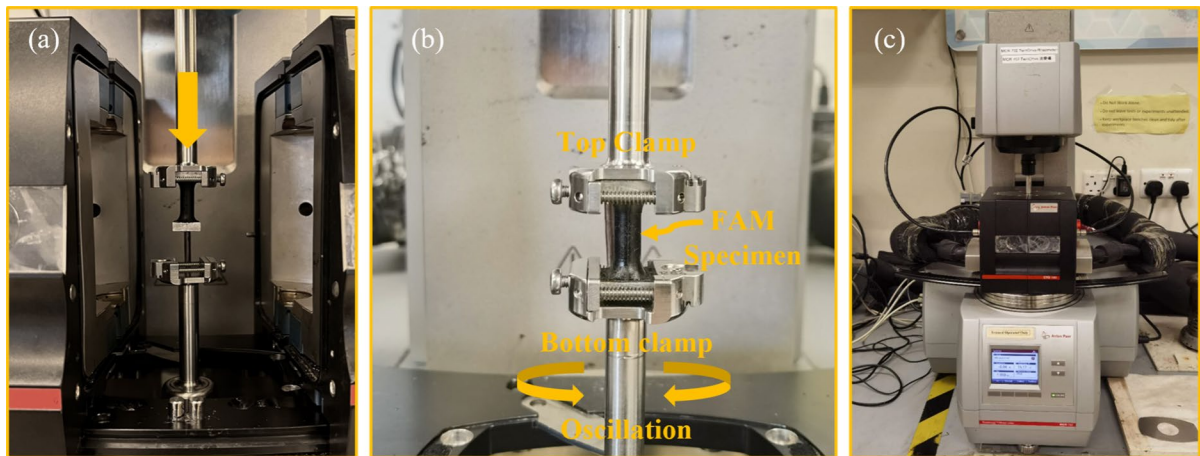

Fig. 6 Measuring system for the fabricated FAM specimen: **a** low-down sample, **b** fix sample and **c** test in progress

one end of the FAM specimen is first fixed on the top fixture via a steel ring. Subsequently, the top fixture is lowered (Fig. 6a) until the bottom steel ring enters the gap of the bottom clamp. By tightening the screw, the specimen can be securely fixed on the machine (Fig. 6b). During testing, the torque applied by the bottom fixture is transferred to the measured FAM material via the steel rings (Fig. 6c).

6.2 Frequency sweep (FS) tests

The FS test is a well-established method for analyzing the LVE properties of FAM. In this study, FS tests were conducted at temperatures ranging from 0 to 50 °C, with a 10 °C interval. Prior to testing, the FAM sample was conditioned at the designated temperature for 15 min to ensure thermal equilibrium throughout the specimen. Subsequently, oscillating shear strain loads with frequencies ranging from 100 to 0.1 Hz were applied. The strain level applied was determined from the LAS test, at which the FAM specimens exhibited linear behavior. Upon completion of the FS testing at one temperature, the temperature was incremented for testing at the next temperature. The FS test data at different temperatures were then utilized to construct a master curve over a wide frequency range using the modified Huet-Sayegh (MHS). An example of the data points from the FS test and the corresponding constructed master curves are presented in Fig. 7.

For further damage analysis, the master curves developed using the MHS model are transformed into Prony series models. The derivation of the parameters for the Prony series model can be referred to in Sect. 2.1. Approximately 13 Maxwell elements in the Prony series model were employed to fit the master curves from 10^{-6} to 10^{6} Hz. The master curves resulting from the fitted Prony series parameters, as determined by Eq. (3) to Eq. (5), are presented in Fig. 8, along with the original master curves developed using the MHS models. It is evident that the optimized Prony series models can closely approximate the original master curves across the entire frequency range, from 10^{-6} to 10^{6} Hz. This good fitting ensures a high degree of accuracy in the subsequent damage analysis.

To assess the repeatability of the FS test across multiple samples, three replicates are employed for each of the three FAMs under investigation. The Mean Percentage Absolute Errors (MPAEs) are calculated for the tested dynamic shear moduli and phase angles for the three FAMs at different temperatures, as depicted in Fig. 9. MPAE represents the average absolute error of all tested data points with respect to their mean values. From Fig. 9, it can be observed that the variability of dynamic shear modulus is higher than that of the phase angle. Additionally, the error is more pronounced at higher temperatures or for the FAM with a higher aggregate content (i.e., FAM(AC20)). Nevertheless, the tests conducted
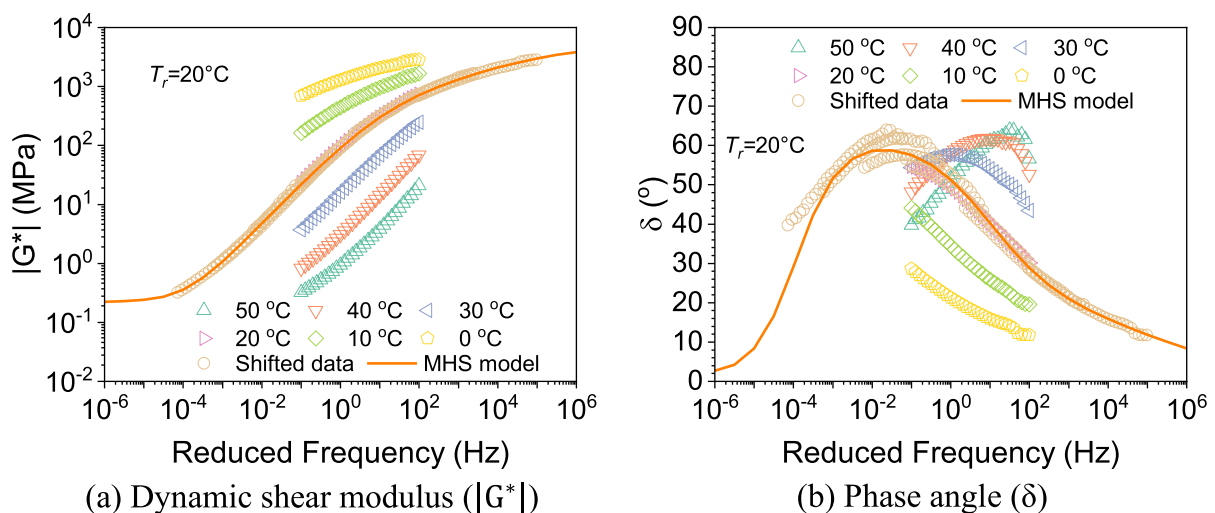

(a) Dynamic shear modulus ($|G^{*}|$)   (b) Phase angle (δ)

Fig. 7 FS test data at different temperatures and the corresponding constructed master curves
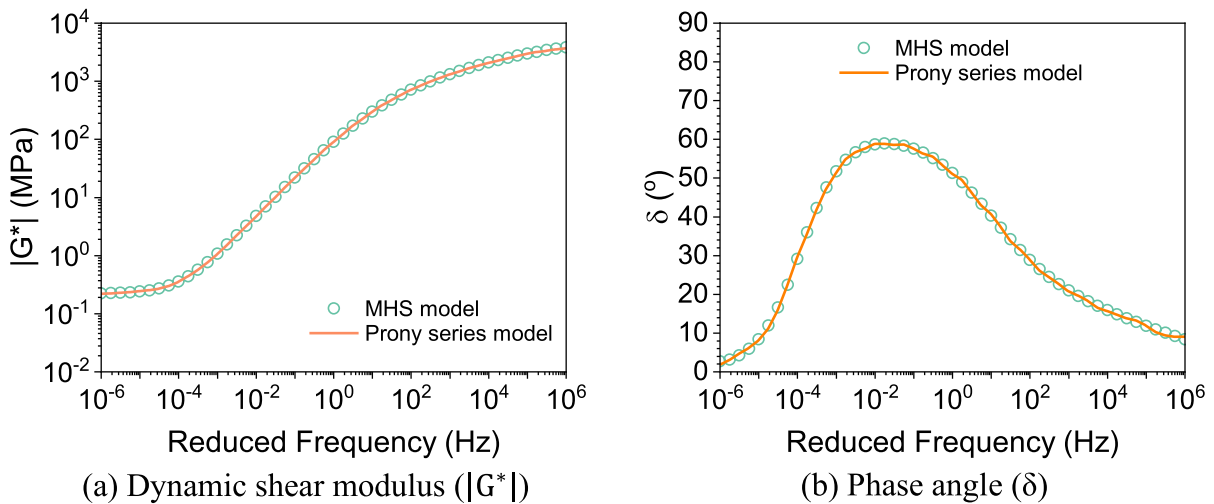
Fig. 8 Master curves constructed by the MHS and Prony series models

(a) Dynamic shear modulus ($|G^*|$)

(b) Phase angle (δ)

Fig. 9 Testing errors of different samples in FS tests
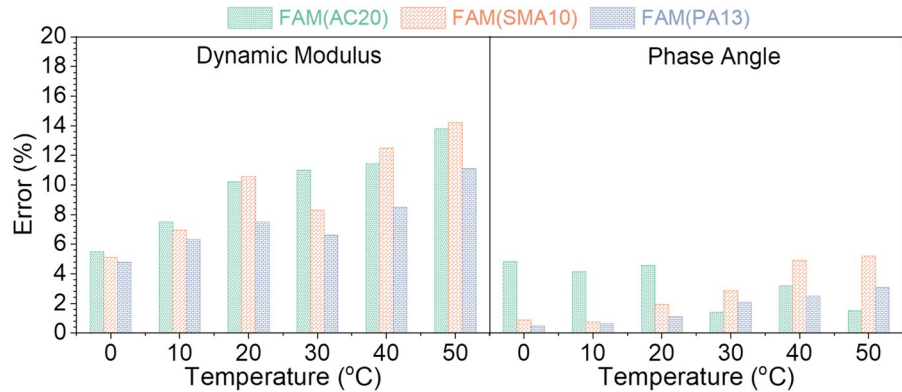
on different samples exhibit good replicability with variations below 15% for dynamic modulus and phase angle within a broad temperature range.

6.3 Linear amplitude sweep (LAS) tests

The linear amplitude sweep (LAS) test is commonly utilized to determine the linear viscoelastic (LVE) range and assess the damage characteristics of FAM. In this study, LAS tests were conducted at a temperature of 20 °C for the three types of FAM. Before testing, each specimen was conditioned at the desired temperature for 20 min. It is worth noting that before conducting the LAS test, the modulus at 10 Hz was measured, which was utilized as the specimen's fingerprint modulus ($|G^*|_{fingerprint}$). During the LAS test, the applied strain was increased linearly from 0.005% to 5%. Figure 10 illustrates the typical curves obtained from the LAS test. In Fig. 10a, the shear stress initially increases with the rise in strain levels, reaching its peak value, and then decreases. The generation and propagation of cracks within the specimen result in a rapid reduction in the stress of the FAM sample. A comparison of the three curves based on the three samples reveals that, at the initiation of the test at small strain levels, the differences are minimal. After the peak stress point, the variations increase for the three samples as damage propagates within the sample, leading to instability. Nevertheless, the variation is still very small. Therefore, it can be confirmed that the LAS test still exhibits
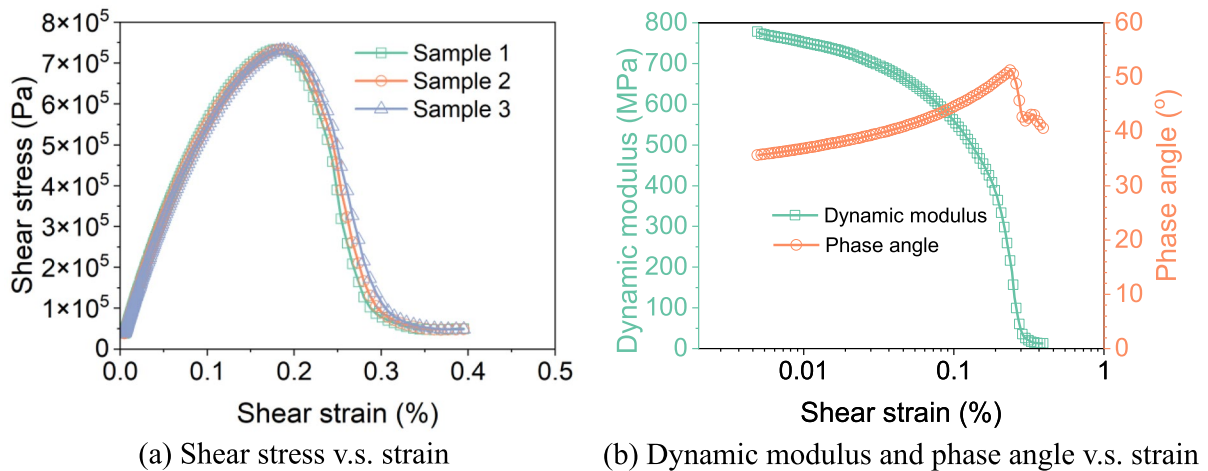
(a) Shear stress v.s. strain

(b) Dynamic modulus and phase angle v.s. strain

Fig. 10 Experimental curves from the LAS test for FAM (AC20)
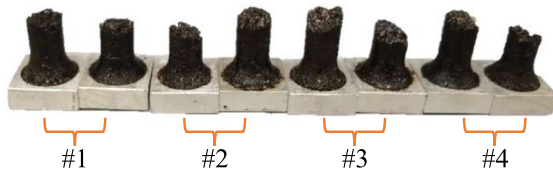

Fig. 11 Example of fractured FAM samples

good repeatability. Additionally, Fig. 10b demonstrates that dynamic shear moduli and phase angles exhibit opposing trends. The dynamic shear moduli gradually decrease while the phase angles increase with increasing strain levels. However, both curves experience a sharp drop in the final stage due to damage accumulation.

Figure 11 displays the four fractured FAM samples after LAS tests, indicating the damage induced by the applied strain. It is evident from the images that all samples are broken in the middle sections, affirming the suitability of the designed geometry for damage testing.

7 Results and discussion

7.1 Master curves

Figure 12 illustrates the constructed master curves for the three types of FAMs. It can be observed that the MHS model adequately characterizes the complex

shear moduli, including dynamic shear moduli ($|G^*|$) and phase angles (δ), over a wide frequency range (10^{-4} Hz to 10^6 Hz). Additionally, the master curves for the three FAMs exhibit distinguishable differences. In the log–log scale, the three FAMs exhibit substantial variations in dynamic moduli at low frequencies, and their differences tend to decrease with increasing frequencies. This finding is predictable since an increase in frequencies stiffens the asphalt binder, reduces the stiffness gap between asphalt binder and aggregate, and weakens the effect of FAM compositions on their viscoelastic properties. Among the three types of FAMs, it is evident from the plots that FAM(AC20) is more elastic (higher shear moduli and lower phase angles) compared to FAM(SMA10) and FAM(PA13). The greater proportion of fine aggregates in FAM(AC20) makes it stiffer than the other two FAMs. The master curves are subsequently converted into Prony series models for further damage analysis.

7.2 Damage characteristic curves

The damage characteristic curves (C-S curves) based on the LAS test are presented in Fig. 13. Figure 13a presents the C-S curves of the three samples of FAM(AC20). These curves show the degradation of pseudo stiffness (C) with increasing damage (S). The closely aligned results of the three calculated C-S curves signify excellent repeatability in the test outcomes. Figure 13b shows the C-S curves for the three
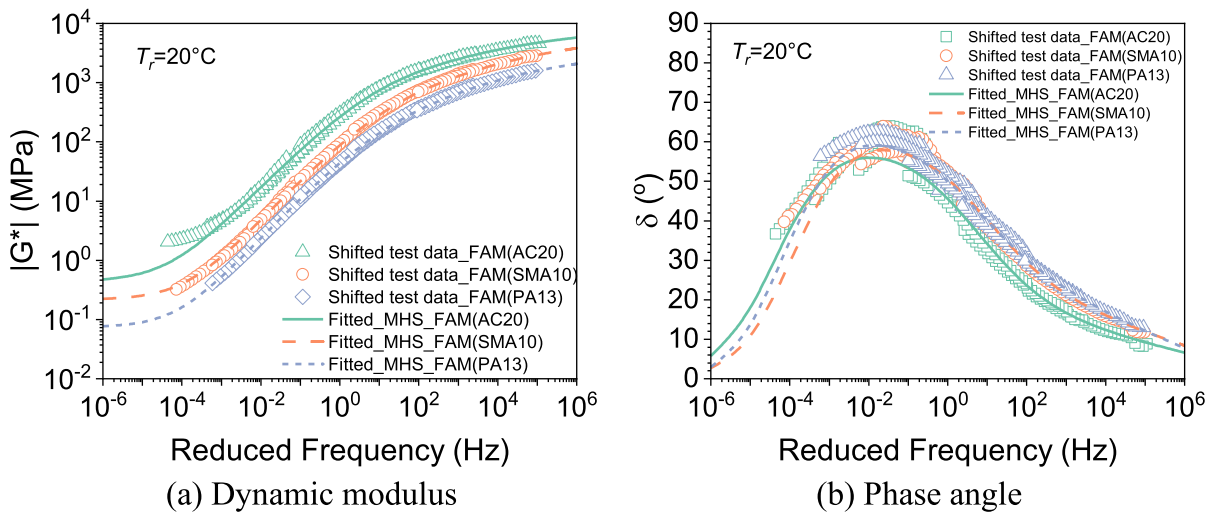
(a) Dynamic modulus   (b) Phase angle

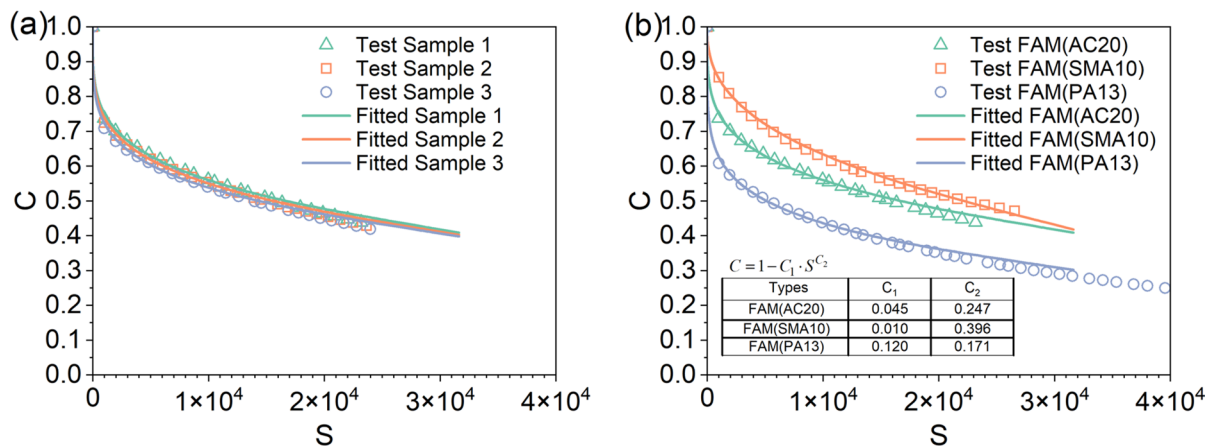**Fig. 12** Constructed master curves of the three types of FAM

Fig. 13 C-S curves of **a** three samples of FAM (AC20); and **b** the three FAMs

FAM types. It can be observed that their C-S curves are significantly different. FAM (PA13) exhibits a more significant reduction in pseudo stiffness at the initial stage, as evidenced by its higher C_1 value, but the slope becomes flatter (lower C_2 value) compared to the other two FAM types with increasing damage. This tendency suggests that FAM(PA13) may have more severe damage at the initial stage, but the rate of damage increase may be much lower with the increase of loading cycles, which may be attributed to FAM(PA13) having a higher fatigue life.

7.3 Fatigue performance characterization

The fatigue life of the three FAMs is calculated based on Eq. (20) and plotted in Fig. 14 against the strain level in the log–log scale. It is observed that the fatigue life decreases with increasing strain levels. The predicted fatigue life curves obtained from the LAS test results effectively distinguish the three FAMs. FAM (PA13) exhibits the highest predicted fatigue life, followed by FAM (SMA10) and FAM(AC20), which is consistent with expectations. The superior fatigue resistance of PA13, an open-graded mixture with a higher asphalt binder content,
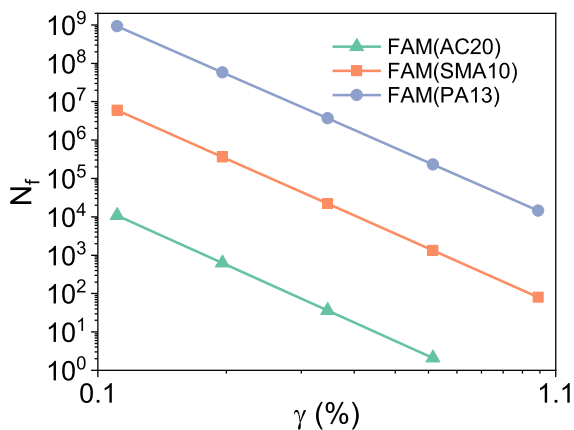
Fig. 14 Predicted curves of fatigue life (N_f) vs. strain (γ)

can be attributed to its lower fine aggregate content. Conversely, the higher fine aggregate content in FAM (AC20) results in significant stress concentration in the aggregate tip zone and contact regions between aggregates, rendering the mastic more susceptible to damage, which consequently characterizes FAM(AC20) with the lowest fatigue life. However, it should be noted that the strain levels of FAM in different asphalt mixtures may vary due to the effects of coarse aggregates. When comparing the fatigue life of asphalt mixtures, it is crucial to consider the actual strain levels experienced by FAM in asphalt mixtures.

8 Conclusions and recommendations

In this study, a new experimental strategy was proposed and applied to evaluate the mechanical properties of three AC mixtures' FAMs. This improved method provided a more accurate representation of the actual FAM in AC and yielded more accurate test results. Additionally, the fatigue properties of FAM were analyzed using the VECD theory. The conclusions drawn from this research are summarized as follows:

The proposed geometry and fabrication methods proved effective in evaluating the viscoelastic and fatigue properties of FAM. Numerical and experimental results demonstrated that the dumbbell-shaped specimen reduced stress concentration at the sample ends, thus improving testing accuracy.

LVE properties of three different types of FAMs were evaluated over a broad frequency range. The FAM with a dense-graded AC mixture (AC20) exhibited greater elasticity compared to gap-graded AC mixture (SMA10) and open-graded AC mixture (PA13), showing higher dynamic moduli and lower phase angles, especially at low frequencies.

VECD theory was adopted to analyze FAM's fatigue properties. theory was employed to analyze FAM's fatigue properties. FAM(PA13) exhibited a faster reduction in pseudo stiffness at the initial stages of damage, with a lower decrease rate as damage increased compared to the other two FAMs.

In future work, CT scanning tests will be performed to comprehensively evaluate the homogeneity of FAM specimens. LAS tests will be conducted at additional temperatures to assess the applicability of the proposed method based on VECD theory. Time sweep tests (cyclic tests at a given strain level) will also be carried out to evaluate the fatigue life of FAM, enabling a comparison with the predicted fatigue life from LAS tests.

Declarations

References

1. Tan Z, Jelagin D, Fadil H et al (2023) Virtual-specimen modeling of aggregate contact effects on asphalt concrete. Constr Build Mater 400:132638. https://doi.org/10.1016/j.conbuildmat.2023.132638

2. Fadil H, Jelagin D, Partl MN (2022) Spherical indentation test for quasi-non-destructive characterisation of asphalt concrete. Mater Struct 55:102. https://doi.org/10.1617/s11527-022-01945-5

3. Leng Z, Tan Z, Cao P, Zhang Y (2021) An efficient model for predicting the dynamic performance of fine aggregate matrix. Comput Civ Infrastruct Eng 36:1467–1479. https://doi.org/10.1111/mice.12706

4. Tan Z, Yang B, Leng Z et al (2023) Multiscale characterization and modeling of aggregate contact effects on asphalt concrete's tension–compression asymmetry. Mater Des 232:112092. https://doi.org/10.1016/j.matdes.2023.112092

5. Tan Z, Guo F, Leng Z et al (2024) A novel strategy for generating mesoscale asphalt concrete model with controllable aggregate morphology and packing structure. Comput Struct 296:107315. https://doi.org/10.1016/j.compstruc.2024.107315

6. Li H, Tan Z, Li R et al (2024) Mechanistic modeling of fatigue crack growth in asphalt fine aggregate matrix under torsional shear cyclic load. Int J Fatigue 178:107999. https://doi.org/10.1016/j.ijfatigue.2023.107999

7. Zhang Y, Leng Z (2017) Quantification of bituminous mortar ageing and its application in ravelling evaluation of porous asphalt wearing courses. Mater Des 119:1–11. https://doi.org/10.1016/j.matdes.2017.01.052

8. Mignini C, Cardone F, Graziani A (2018) Experimental study of bitumen emulsion–cement mortars: mechanical behaviour and relation to mixtures. Mater Struct 51:149. https://doi.org/10.1617/s11527-018-1276-y

9. Yan Y, Hernando D, Lopp G et al (2018) Enhanced mortar approach to characterize the effect of reclaimed asphalt pavement on virgin binder true grade. Mater Struct 51:41. https://doi.org/10.1617/s11527-018-1168-1

10. Gudipudi PP, Underwood BS (2017) Development of modulus and fatigue test protocol for fine aggregate matrix for axial direction of loading. J Test Eval 45:497–508

11. Tan Z, Leng Z, Jelagin D et al (2023) Numerical modeling of the mechanical response of asphalt concrete in tension and compression. Mech Mater 187:104823. https://doi.org/10.1016/j.mechmat.2023.104823

12. Bhasin A, Little DN, Bommavaram R, Vasconcelos K (2008) A framework to quantify the effect of healing in bituminous materials using material properties. Road Mater Pavement Des 9:219–242. https://doi.org/10.1080/14680629.2008.9690167

13. Ding J, Jiang J, Han Y et al (2022) Rheology, chemical composition, and microstructure of the asphalt binder in fine aggregate matrix after different long-term laboratory aging procedures. J Mater Civ Eng 34:04022014. https://doi.org/10.1061/(ASCE)MT.1943-5533.0004147

14. Riccardi C, Cannone Falchetto A, Losa M, Wistuba MP (2016) Rheological modeling of asphalt binder and asphalt mortar containing recycled asphalt material. Mater Struct 49:4167–4183. https://doi.org/10.1617/s11527-015-0779-z

15. Jiao L, Elkashef M, Harvey JT et al (2022) Investigation of fatigue performance of asphalt mixtures and FAM mixes with high recycled asphalt material contents. Constr Build Mater 314:125607. https://doi.org/10.1016/j.conbuildmat.2021.125607

16. Li H, Huang Y, Yang Z et al (2022) 3D meso-scale fracture modelling of concrete with random aggregates using a phase-field regularized cohesive zone model. Int J Solids Struct 256:111960. https://doi.org/10.1016/j.ijsolstr.2022.111960

17. Sun B, Hao P, Zhang H, Liu J (2022) Establishment and verification of a developed viscoelastic damage model and creep instability criterion for modified fine asphalt mortar. Mater Struct 55:107. https://doi.org/10.1617/s11527-022-01951-7

18. Ding J, Jiang J, Ni F et al (2020) Correlation investigation of fatigue indices of fine aggregate matrix (FAM) and asphalt mixture containing reclaimed asphalt pavement materials. Constr Build Mater 262:120646. https://doi.org/10.1016/j.conbuildmat.2020.120646

19. Osmari PH, de Souza RC, do Nascimento LAH, Aragão FTS, (2020) Evaluation of the relationship between the fatigue performance of FAM and AC mixtures based on volumetric characteristics and on the S-VECD theory. Constr Build Mater 265:120294. https://doi.org/10.1016/j.conbuildmat.2020.120294

20. Song W, Deng Z, Wu H, Xu Z (2023) Cohesive zone modeling of I-II mixed mode fracture behaviors of hot mix asphalt based on the semi-circular bending test. Theor Appl Fract Mech 124:103781. https://doi.org/10.1016/j.tafmec.2023.103781

21. Li H, Luo X, Gu Z et al (2023) Predicting crack growth of paving materials under indirect tensile fatigue loads. Int J Fatigue 175:107818. https://doi.org/10.1016/j.ijfatigue.2023.107818

22. Li H, Luo X, Zhang Y, Leng Z (2023) Viscoelastic fracture mechanics-based fatigue life model in asphalt-filler composite system. Eng Fract Mech 292:109589. https://doi.org/10.1016/j.engfracmech.2023.109589

23. Cao P, Jin F, Zhou C et al (2016) Steady-state dynamic method: An efficient and effective way to predict dynamic modulus of asphalt concrete. Constr Build Mater 111:54–62. https://doi.org/10.1016/j.conbuildmat.2016.02.071

24. Underwood BS, Kim YR (2013) Microstructural association model for upscaling prediction of asphalt concrete dynamic modulus. J Mater Civ Eng 25:1153–1161. https://doi.org/10.1061/(ASCE)MT.1943-5533.0000657

25. Tan Z, Leng Z, Jiang J et al (2022) Numerical study of the aggregate contact effect on the complex modulus of asphalt concrete. Mater Des 213:110342. https://doi.org/10.1016/j.matdes.2021.110342

26. Du C, Liu P, Oeser M (2022) Homogenization of the elastic-viscoplastic damage behavior of asphalt mixtures based on the mesomechanical Mori-Tanaka method. Eng Comput. https://doi.org/10.1007/s00366-022-01628-3

27. Yao L, Leng Z, Jiang J et al (2023) Effects of traffic load amplitude sequence on the cracking performance of asphalt pavement with a semi-rigid base. Int J Pavement

Eng 24:2152027. https://doi.org/10.1080/10298436.2022.2152027

28. Cheng H, Sun L, Wang Y, Chen X (2021) Effects of actual loading waveforms on the fatigue behaviours of asphalt mixtures. Int J Fatigue 151:106386. https://doi.org/10.1016/j.ijfatigue.2021.106386

29. Cao P, Leng Z, Shi F et al (2020) A novel visco-elastic damage model for asphalt concrete and its numerical implementation. Constr Build Mater 264:120261. https://doi.org/10.1016/j.conbuildmat.2020.120261

30. Li H, Luo X, Zhang Y, Xu R (2021) Stochastic fatigue damage in viscoelastic materials using probabilistic pseudo J-integral Paris' law. Eng Fract Mech 245:107566. https://doi.org/10.1016/j.engfracmech.2021.107566

31. Li H, Luo X, Yan W, Zhang Y (2020) Energy-based mechanistic approach for crack growth characterization of asphalt binder. Mech Mater 148:103462. https://doi.org/10.1016/j.mechmat.2020.103462

32. Li D, Leng Z, Zhang S et al (2022) Blending efficiency of reclaimed asphalt rubber pavement mixture and its correlation with cracking resistance. Resour Conserv Recycl 185:106506. https://doi.org/10.1016/j.resconrec.2022.106506

33. Little DN, Allen DH, Bhasin A (2018) Modeling and design of flexible pavements and materials. Springer International Publishing, Cham

34. Zhang YFC, de Ven M, Molenaar AAA, Wu S (2016) Assessment of effectiveness of rejuvenators on artificially aged mortar. J Mater Civ Eng 28:04016079. https://doi.org/10.1061/(ASCE)MT.1943-5533.0001582

35. Smith BJ, Hesp SAM (2000) Crack pinning in asphalt mastic and concrete: regular fatigue studies. Transp Res Rec 1728:75–81. https://doi.org/10.3141/1728-11

36. Fang C, Guo N, Leng Z et al (2022) Kinetics-based fatigue damage investigation of asphalt mixture through residual strain analysis using indirect tensile fatigue test. Constr Build Mater 352:128962. https://doi.org/10.1016/j.conbuildmat.2022.128962

37. Zhang Z, Oeser M (2020) Residual strength model and cumulative damage characterization of asphalt mixture subjected to repeated loading. Int J Fatigue. https://doi.org/10.1016/j.ijfatigue.2020.105534

38. Li Q, Chen X, Li G, Zhang S (2018) Fatigue resistance investigation of warm-mix recycled asphalt binder, mastic, and fine aggregate matrix. Fatigue Fract Eng Mater Struct 41:400–411. https://doi.org/10.1111/ffe.12692

39. Zhang Z, Oeser M (2021) Energy dissipation and rheological property degradation of asphalt binder under repeated shearing with different oscillation amplitudes. Int J Fatigue 152:106417. https://doi.org/10.1016/j.ijfatigue.2021.106417

40. Margaritis A, Pipintakos G, Varveri A et al (2021) Towards an enhanced fatigue evaluation of bituminous mortars. Constr Build Mater 275:121578. https://doi.org/10.1016/j.conbuildmat.2020.121578

41. Shen S, Airey GD, Carpenter SH, Huang H (2006) A dissipated energy approach to fatigue evaluation. Road Mater Pavement Des 7:47–69. https://doi.org/10.1080/14680629.2006.9690026

42. Ghuzlan KA, Carpenter SH (2000) Energy-derived, damage-based failure criterion for fatigue testing. Transp Res Rec 1723:141–149. https://doi.org/10.3141/1723-18

43. Kutay ME, Lanotte M (2018) Viscoelastic continuum damage (VECD) models for cracking problems in asphalt mixtures. Int J Pavement Eng 19:231–242. https://doi.org/10.1080/10298436.2017.1279492

44. Wang C, Gong G, Ren Z (2023) Addressing the healing compensation on fatigue damage of asphalt binder using TSH and LASH tests. Int J Fatigue 167:107292. https://doi.org/10.1016/j.ijfatigue.2022.107292

45. Wang C, Sun Y, Ren Z (2023) Toward to a viscoelastic fatigue and fracture model for asphalt binder under cyclic loading. Int J Fatigue 168:107479. https://doi.org/10.1016/j.ijfatigue.2022.107479

46. Hou T, Underwood BS, Kim YR (2010) Fatigue performance prediction of North Carolina mixtures using the simplified viscoelastic continuum damage model. J Assoc Asph Paving Technol 79:35–73

47. Wang C, Castorena C, Zhang J, Richard Kim Y (2015) Unified failure criterion for asphalt binder under cyclic fatigue loading. Road Mater Pavement Des 16:125–148. https://doi.org/10.1080/14680629.2015.1077010

48. Wang Y, Richard Kim Y (2019) Development of a pseudo strain energy-based fatigue failure criterion for asphalt mixtures. Int J Pavement Eng 20:1182–1192. https://doi.org/10.1080/10298436.2017.1394100

49. Sadeq M, Al-Khalid H, Masad E, Sirin O (2016) Comparative evaluation of fatigue resistance of warm fine aggregate asphalt mixtures. Constr Build Mater 109:8–16. https://doi.org/10.1016/j.conbuildmat.2016.01.045

50. Coutinho R, Castelo Branco VTF, Babadopulos L, Soares J (2013) The use of linear amplitude sweep tests to characterize fatigue damage in fine aggregate matrices. In: 1st conference on rheology and processing of construction materials. Paris, France

51. Behbahani H, Salehfard R (2021) A review of studies on asphalt fine aggregate matrix. Arab J Sci Eng 46:10289–10312. https://doi.org/10.1007/s13369-021-05479-w

52. Sousa P, Kassem E, Masad E, Little D (2013) New design method of fine aggregates mixtures and automated method for analysis of dynamic mechanical characterization data. Constr Build Mater 41:216–223. https://doi.org/10.1016/j.conbuildmat.2012.11.038

53. Freire RA, Freire AL, Babadopulos LTF, Castelo Branco V, Bhasin A (2017) Aggregate maximum nominal sizes' influence on fatigue damage performance using different scales. J Mater Civ Eng 29:04017067. https://doi.org/10.1061/(ASCE)MT.1943-5533.0001912

54. Im S, You T, Ban H, Kim Y-R (2017) Multiscale testing-analysis of asphaltic materials considering viscoelastic and viscoplastic deformation. Int J Pavement Eng 18:783–797. https://doi.org/10.1080/10298436.2015.1066002

55. Castelo Branco VTF (2009) A unified method for the analysis of nonlinear viscoelasticity and fatigue cracking of asphalt mixtures using the dynamic mechanical analyzer

56. Ng AKY, Vale AC, Gigante AC, Faxina AL (2018) Determination of the binder content of fine aggregate matrices prepared with modified binders. J Mater Civ Eng 30:04018045. https://doi.org/10.1061/(ASCE)MT.1943-5533.0002160

57. Suresha SN, Ningappa A (2018) Recent trends and laboratory performance studies on FAM mixtures: a state-of-the-art review. Constr Build Mater 174:496–506. https://doi.org/10.1016/j.conbuildmat.2018.04.144

58. Jiang J, Li Y, Zhang Y, Bahia HU (2022) Distribution of mortar film thickness and its relationship to mixture cracking resistance. Int J Pavement Eng 23:824–833. https://doi.org/10.1080/10298436.2020.1774767

59. Caro S, Sánchez DB, Caicedo B (2015) Methodology to characterise non-standard asphalt materials using DMA testing: application to natural asphalt mixtures. Int J Pavement Eng 16:1–10. https://doi.org/10.1080/10298436.2014.893328

60. Zhao Z, Jiang J, Ni F, Ma X (2021) 3D-Reconstruction and characterization of the pore microstructure within the asphalt FAM using the x-ray micro-computed tomography. Constr Build Mater 272:121764. https://doi.org/10.1016/j.conbuildmat.2020.121764

61. Huurman RM, Mo L, Woldekidan MF (2010) Unravelling porous asphalt concrete towards a mechanistic material design tool. Road Mater Pavement Des 11:583–612. https://doi.org/10.1080/14680629.2010.9690295

62. Palvadi S, Bhasin A, Little DN (2012) Method to quantify healing in asphalt composites by continuum damage approach. Transp Res Rec 2296:86–96. https://doi.org/10.3141/2296-09

63. Underwood BS, Kim YR (2013) Effect of volumetric factors on the mechanical behavior of asphalt fine aggregate matrix and the relationship to asphalt mixture properties. Constr Build Mater 49:672–681. https://doi.org/10.1016/j.conbuildmat.2013.08.045

64. Lakes RS (1998) Viscoelastic solids. CRC Press

65. Bergström J (2015) Mechanics of solid polymers: theory and computational modeling. Elsevier, New Jersey, p 102

66. Williams ML (1964) Structural analysis of viscoelastic materials. AIAA J 2:785–808. https://doi.org/10.2514/3.2447

67. Ferry JD (1980) Viscoelastic properties of polymers, 3rd edn. Wiley, NJ

68. Woldekidan MF, Huurman M, Pronk AC (2012) A modified HS model: numerical applications in modeling the response of bituminous materials. Finite Elem Anal Des 53:37–47. https://doi.org/10.1016/j.finel.2012.01.003

69. Pronk AC (2012) The Huet-sayegh model: a simple and excellent rheological model for master curves of asphaltic mixes. Finite Elem Analy Des 53:73–82. https://doi.org/10.1061/40825(185)8

70. Chen X, Wang Y, Wen Y et al (2023) Quantitative analysis of oxidative aging effects on the fatigue resistance of asphalt mixtures based on the simplified viscoelastic continuum damage (S-VECD) model. Int J Fatigue 177:107916. https://doi.org/10.1016/j.ijfatigue.2023.107916

71. Schapery RA (1984) Correspondence principles and a generalized J integral for large deformation and fracture analysis of viscoelastic media. Int J Fract 25:195–223. https://doi.org/10.1007/BF01140837

72. Park SW, Schapery RA (1997) A viscoelastic constitutive model for particulate composites with growing damage. Int J Solids Struct 34:931–947. https://doi.org/10.1016/S0020-7683(96)00066-2

73. Kim YR, Lee HJ, Kim Y, Little DN (1997) Mechanistic evaluation of fatigue damage growth and healing of asphalt concrete: laboratory and field experiments. In: eighth international conference on asphalt pavements federal highway administration

74. Chen H, Zhang Y, Bahia HU (2021) Estimating asphalt binder fatigue at multiple temperatures using a simplified pseudo-strain energy analysis approach in the LAS test. Constr Build Mater 266:120911. https://doi.org/10.1016/j.conbuildmat.2020.120911

75. ASTM E466 (2021) Standard practice for conducting force controlled constant amplitude axial fatigue tests of metallic materials

76. Apostolidis P, Liu X, Daniel GC et al (2020) Effect of synthetic fibres on fracture performance of asphalt mortar. Road Mater Pavement Des 21:1918–1931. https://doi.org/10.1080/14680629.2019.1574235

77. Apostolidis P, Liu X, Scarpas A et al (2016) Advanced evaluation of asphalt mortar for induction healing purposes. Constr Build Mater 126:9–25. https://doi.org/10.1016/j.conbuildmat.2016.09.011

78. Underwood BS, Kim YR (2013) Microstructural investigation of asphalt concrete for performing multiscale experimental studies. Int J Pavement Eng 14:498–516. https://doi.org/10.1080/10298436.2012.746689